The role of porosity and acidity in the catalytic upcycling of polyethylene

The role of porosity and acidity in the catalytic upcycling of polyethylene

Valeria Finelli, Valentina Gentilin, Giulia Mossotti, Gabriele Ricchiardi, Alessandro Piovano, Valentina Crocellà, Elena Groppo

PII: S0920-5861(23)00166-9

DOI: https://doi.org/10.1016/j.cattod.2023.114142

Reference: CATTOD114142

To appear in: *Catalysis Today*

Received date: 14 December 2022
Revised date: 10 March 2023
Accepted date: 1 April 2023

Please cite this article as: Valeria Finelli, Valentina Gentilin, Giulia Mossotti, Gabriele Ricchiardi, Alessandro Piovano, Valentina Crocellà and Elena Groppo, The role of porosity and acidity in the catalytic upcycling of polyethylene, *Catalysis Today,* (2023) doi:https://doi.org/10.1016/j.cattod.2023.114142

The role of porosity and acidity in the catalytic upcycling of polyethylene

Valeria Finelli,[a,b] Valentina Gentilin,[a] Giulia Mossotti,[c,a] Gabriele Ricchiardi,[a] Alessandro Piovano,[c,a,*] Valentina Crocellà,[a,*] Elena Groppo[a]

[a] Department of Chemistry, NIS and INSTM Reference Centre, Università di Torino, Via G. Quarello 15/A, I-10135, and Via P. Giuria 7, I-10125, Turin - Italy

[b] Istituto Universitario degli Studi Superiori (IUSS), Palazzo del Broletto, Piazza della Vittoria 15, I-27100, Pavia - Italy

[c] Department of Applied Science and Technology (DISAT), Politecnico di Torino, Corso Duca degli Abruzzi 24, I-10129, Turin - Italy

Abstract

Plastics have become fundamental and widespread materials in our everyday life. Nowadays, the most demanded plastics are polyolefins, accounting for nearly half of the Global plastic production. However, the end-of-life disposal of these materials is an inevitably issue connected to their increased production. Among chemical recycling techniques, the most thoroughly investigated process is the catalytic pyrolysis, showing a vast panorama of different set-ups optimized for the major production of either gaseous or liquid compounds.

In this contribution a series of mesoporous silica-based materials, either pure SiO_2 or substituted with Zr and Al, were systematically synthetized varying both porous framework and surface acidity, in the attempt of rationalizing the effect of each parameter (deeply characterized by physico-chemical methods) on the catalytic pyrolysis of linear low-density polyethylene (LLDPE). The synthetized materials together with some zeolites and aluminas reference samples were tested towards LLDPE degradation in a batch reactor set-up optimized for the formation and accumulation of the gaseous compounds, coupled with IR spectroscopy for in situ monitoring the evolution of the most abundant species (mostly propylene and branched C4-C6 olefins, together with a minor fraction of ethylene and short hydrocarbons). This work points out the necessity of the presence of Brønsted acid sites for a good activity (in terms of both the yield of gaseous products and lowering of the process temperature), but it also reveals a non-negligible role of the Lewis acid sites and it warns about the importance of controlling not only the amount of acid sites but also their strength.

Graphical Abstract

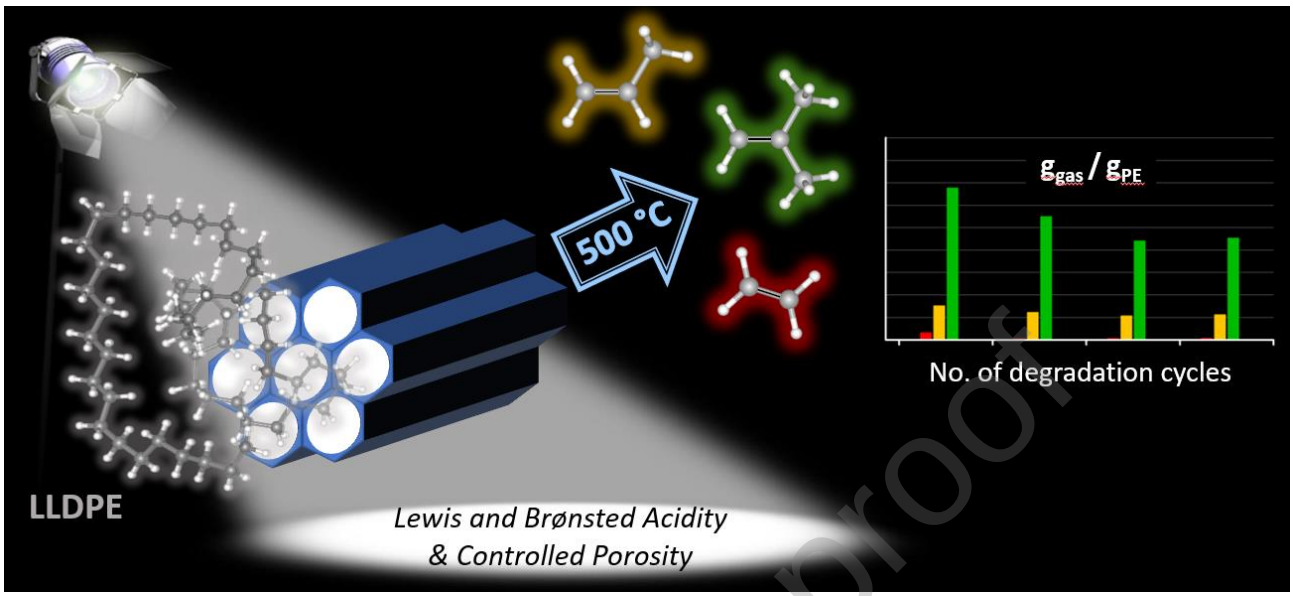

1. INTRODUCTION

Plastics have become fundamental and widespread materials in our everyday life, because of their excellent properties, such as high formability, low density, durability, high versatility, and relatively low cost. Plastics possess good hygienic properties, making them the best choice for single use items in the medical field and for food packaging, allowing a longer food conservation. Their low density implies that they are extremely lightweight materials compared to glasses or metals, making them the key materials for the development of the mobility sector, having a lower impact on energy consumption and CO_2 emissions [1]. For all these reasons, plastics are unique and irreplaceable in many applications.

By far, the most demanded plastics are polyolefins (POs), accounting for nearly half of the World plastic production (equal to 390.7 Mt in 2021) [2–4]. The end-of-life disposal of these materials is an inevitable issue connected to their increased production: a very low fraction of POs recycled at the end of life represents a clear loss in the plastic market loop and creates environmental concerns. About 95% of POs ends up as a waste after finishing their (short) lifetime, contributing to more than 60% of the total plastic content of municipal solid waste. Unimaginable quantities of POs end up in the oceans every year, and minuscule particles find their way into the atmosphere, the soil, and the rivers [5]. At the beginning of 2018 EU launched the “European Strategy for Plastics in a Circular economy”, which promotes circularity for the most widely used plastics [6]. Chemical recycling methods are the only ones allowing the true circularity of plastic materials [7–11]. Even though the initial monomers recovery is the “holy grail” of POs chemical recycling [12], the production of fuels starting from POs waste is also attractive especially in the actual geopolitical situation, which has reignited the importance of energy resources alternative to petroleum-based fuels.

One of the most consolidated approaches is thermal pyrolysis [13,14]. Pyrolysis of plastic waste is typically conducted under severe reaction conditions (inert atmosphere, temperature above 450 °C), which induce the homolytic cleavage of the polymer chains, yielding radical fragments that undergo unselective secondary reactions. The result is a broad mixture of hydrocarbons, the pyrolysis oil, which must be upgraded by hydrogenation before processing by steam cracking, where ethylene (and propylene) monomers are obtained, to be used in the production of new POs with the same properties of fossil-based POs. This approach has the advantage to be unselective compared to the plastic waste, contributing to re-using those post-consumer plastics that are difficult to recycle mechanically. However, two important drawbacks

affect the economics of the process: it requires very high temperatures and two subsequent steps (i.e., thermal pyrolysis + hydrogenation).

An alternative well-established approach for the upcycle of POs is catalytic pyrolysis: this process converts the long PO chains into shorter ones, producing gaseous (C1-C4) and/or liquid (C5-C12) hydrocarbons (both alkanes and olefins), aromatics, and waxes (over C20) [15], in the presence of a solid acid catalyst (containing either Lewis acid sites, LAS, or Brønsted ones, BAS, or even both) [16,17] at still high temperature (usually above 300 - 400 °C) through a carbocationic mechanism [9]. Even though the catalytic pyrolysis of POs waste is technically feasible and has been already implemented at industrial level [18–22], the elevated temperatures raise the challenge of selectivity control and catalyst fast deactivation, which decrease its competitiveness with respect to thermal pyrolysis. To complicate the scenario, not only the temperatures, but also the reactor design as well as the catalyst itself strongly affects the selectivity of the reaction, making the comparison of the results reported in the literature difficult. Limiting the discussion to the processes carried out at temperatures lower than 500 °C, the panorama is extremely varied and complex, including fluidized-bed reactors optimized for both liquid products [23,24] and gaseous fractions [25,26], two-steps thermal-catalytic processes favouring both gases [27,28] and liquids [14,24], fixed-bed reactors with tuneable liquid/gas ratio depending on the residence time [29], and batch reactors for obtaining gasoline fraction [23,30,31]. In most of the cases, the catalysts are either zeolites, or heteroatom-substituted silicas and aluminas, containing either Brønsted or Lewis acid sites, or even both, and they are characterized by different porosities [32].

In the attempt of rationalizing the role of the catalyst in the catalytic pyrolysis of POs, we carried out a systematic work on a series of Zr and Al-substituted mesoporous silicas, characterized by different porous frameworks (effect of Zr insertion) and different acidities (effect of Al insertion). The materials have been synthetized, characterized in depth by means of a multi-technique physical-chemical approach and tested in the upcycling of a commercial LLDPE sample. The catalytic performances were evaluated in terms of degradation temperature and volatile products, the latter identified with GC-MS and quantified by IR spectroscopy, adopting a simple and versatile experimental set-up optimized for the detection of volatile products. The obtained results were compared with those obtained in the presence of the following materials, chosen as reference catalysts: protonic zeolite H-ZSM-5, Al_2O_3, and sulphated Al_2O_3.

2. EXPERIMENTAL

2.1. The catalysts

2.1.1 Synthesis of mesoporous silicas

Six different ordered mesoporous silicas of the SBA family (namely SBA-15, Zr-SBA-15 and Al-SBA-15, and SBA-16, Zr-SBA-16, and Al-SBA-16) were synthesised to be successively used in the catalytic upcycling of LLDPE. Zr and Al were inserted in the siliceous framework through a one-pot synthesis procedure, i.e., by directly mixing both tetraethyl orthosilicate (TEOS) and the metal precursors in the starting synthesis gel. The metal-substituted silicas were synthetized with the same metal/Si molar ratio (0.035, corresponding to a Si/metal ratio of 29). All the syntheses were performed according to procedures already reported in the literature [33–37] (see SI, section S1 for further details on reaction times and temperatures). Briefly, the synthesis consists of three main steps: i) the gelation of the precursor(s) was conducted in a round bottom flask equipped with a condenser ~~(necessary to prevent the evaporation of the solvent and to maintain the nominal composition) and inserted in an oil bath for thermostatic regulation)~~; ii) the hydrothermal treatment was performed in a Teflon lined stainless steel digestor of 125 ml volume, heated in an oven under static conditions; iii) the pyrolysis of the materials was performed in a tubular oven at a heating ramp of 2°C/min up to 550 °C in N_2 flow, to carbonize the organic template without collapsing the structure of the material, and it was followed by their calcination in O_2 at 550 °C in isothermal conditions for 7 h to burn the carbonaceous phase. Only the synthesis of Al-SBA-16 silica was performed without any hydrothermal treatment (step ii) and its mixture was kept stirring under reflux conditions. The complete synthesis procedures are reported in detail in the Supporting Information.

The actual chemical composition of the synthesised materials was experimentally evaluated by means of EDX elemental microanalysis and it is in agreement with the expected nominal one, as shown by Table S1.

2.1.2 Reference catalysts

Different commercial materials have been used as reference catalysts. A commercial ZSM-5 zeolite (Si/Al = 15) in the ammonic form was provided by Zeolyst and converted into the protonic form by thermal treatment at high temperature (500 °C in vacuum) when needed. The protonic acid zeolite is hereafter referred to as H-ZSM-5. Commercial γ-Al_2O_3 (boehmite) sample and its sulphated

counterpart was obtained by contacting γ-Al_2O_3 with a 0.5 M solution of $(NH_4)_2SO_4$ via incipient wetness impregnation as reported in ref. [38].

2.2. Catalysts characterization

2.2.1 Structure, morphology, and composition

Powder X-Ray Diffraction (PXRD) patterns of the mesoporous silicas were collected on a PANalytical X' Pert instrument with Cu K_α radiation corresponding to an incident wavelength λ=1.5405 Å. The patterns were acquired in the 2θ range of 0.5-5° (low angles) and 5-80° (high angles), using the Bragg-Brentano geometry.

Field Emission Scanning Electron Microscopy (FE-SEM) images were collected using a TESCAN S9000G microscope equipped with a FEG type Schottky electron source working at 10 kV of electron accelerating potential, with the detector for secondary electrons In-Beam SE, with resolution 0.7 nm at 15 kV. The not conductive samples were fixed to a metallic stub with carbon tape and sputtered with a 2 nm thin Cr-coat to enhance their conductibility. Transmission Electron Microscopy (TEM) analysis was conducted on a TEM JEOL JEM 3010 UHR microscope (with 0.17 nm of theoretical resolution) equipped with a lanthanum hexaboride LaB_6 electron source working at 300 kV electron accelerating potential.

Energy Dispersive X-Ray (EDX) microanalysis was performed thanks to an OXFORD X-STREAM energy dispersion detector, software INCA. The images were collected by a CCD camera Gatan, Model 894 US1000 (2k x 2k). The samples were prepared depositing a small amount of powder over a 200 mesh lacey carbon copper grid.

2.2.2 Textural properties

Volumetric measurements were performed on a Micromeritics 3FLEX instrument in order to evaluate the textural properties of the porous catalysts. N_2 adsorption-desorption isotherms were measured at liquid N_2 temperature. The textural properties were evaluated by using the software Microactive provided by Micromeritics. The Specific Surface Areas (SSAs) of the samples were calculated using the Branauer-Emmet-Teller (BET) equation in the 0.05-0.17 p/p^0 range for the SBA-15 materials and in the 0.05-0.11 p/p^0 range for the SBA-16 ones. The linear BET fits are displayed in Figure S8, and they are limited to these ranges to keep $2 < C$ constant < 200 for N_2 physisorption, according to the BET theory. In particular, for the SBA-16 materials the Rouquerol consistency criteria [39] were adopted to maintain C value < 200. The cumulative pore volume and the pore size distribution were evaluated using both the Barrett-Joyner-Halenda (BJH) method,

considering Halsey as thickness curve and Faas as BJH correction, and the Non-Local Density Functional Theory (NL-DFT), using cylindrical pore geometry and the "N_2 Cylindrical Pores Oxide Surfaces" model. Being conscious that the cylindrical pore geometry is not the optimal choice to model the spherical pores of the SBA-16 materials, however it reveals as the closest geometry option present at the moment. The goodness of the so-obtained pore size distribution was evaluated by comparing the goodness of fitting graphs of the experimental isotherms obtained with various models. The NL-DFT pore size logarithmic goodness of fit graphs are shown in Figures S9-11 for all the materials to control their behaviour especially in the micropores region.

2.2.3 Evaluation of the acidity

FT-IR spectroscopy was carried out on a Bruker Vertex 70 spectrophotometer, equipped with a DTGS detector and a Globar IR source. All the spectra were collected at a resolution of 2 cm^{-1}, averaging 32 scans per spectrum. The samples were analysed in the form of self-supporting pellets (with an optical density of ca. 10-20 mg/cm^2), inserted into a gold envelop and placed in a quartz cell equipped with CaF_2 windows. Prior each analysis, the samples were degassed under dynamic vacuum while heating up to 500 °C (5 °C/min heating ramp). Once the target temperature was reached, two dosages of ca. 200 mbar of O_2 were kept in contact with the samples for 30 minutes to eliminate all the eventual organic residues, followed by degassing under dynamic vacuum to remove all the by-products. Adsorption of pyridine monitored by FT-IR spectroscopy was performed to quantify the acidic surface sites of the materials. After collecting an IR spectrum, the activated catalyst was exposed to pyridine vapour pressure at room temperature. After reaching pyridine maximum coverage, a series of IR spectra were collected during evacuation at room temperature. Then the pellet was degassed at 200 °C for 1 hour to ensure the remotion of all the physisorbed fraction and keep only the strongly interacting adsorbed pyridine. The IR spectrum collected after this step was used to quantify the amount of acid sites on each sample, following a well-established procedure (vide infra) [40].

2.3. Thermo-catalytic upcycling of LLDPE

All the degradation tests were performed on a commercial LLDPE sample, from Versalis S.p.A., named Flexirene FG 30 U. It is a butene-ethylene copolymer (C4-LLDPE), suitable for blown film extrusion, supplied in pellets. Its declared melting temperature is between 190 °C and 230 °C, and its density is 0.925 g/cm^3. The finely chopped polymer and the catalyst in the powder form were mixed in a 1:1 ratio for all the experiments.

2.3.1 TGA measurements

Thermo-gravimetric analyses (TGA) were performed on an SDT-Q600 instrument under N_2 flow, increasing the temperature up to 500 °C with a heating ramp of 5 °C/min. They allowed the determination of the temperature at which the degradation starts (T_{start}) and the one at which it proceeds at the fastest rate (T_{max}, evaluated as the maximum of the first derivative curve).

2.3.2 TPD-IR measurements complemented by GC-MS

Temperature Programmed Degradation coupled to IR spectroscopy (TPD-IR) experiments were conducted with a custom-made set-up [41] composed by: i) a quartz reactor, ii) an oven, iii) an IR cell with an optical path of 17 cm, designed for the detection of gases, iv) a valve to isolate the system, and v) a vacuum line. The quartz reactor was connected to the IR cell, and the IR cell to the vacuum line, through small diameter plastic tubes via Swagelok connections to ensure flexibility to the entire system. The IR cell was placed into the sample compartment of the spectrophotometer to monitor the gaseous products. In a typical experiment, the LLDPE + catalyst mixture (approx. 25-50 mg, 1:1 mass ratio) is placed in the reactor: differently from common practice [42,43], an equal amount of LLDPE and catalyst was considered to understand the role that also weakly active catalysts could play in LLDPE degradation. The mixture is heated up at 150 °C under dynamic vacuum overnight to remove physisorbed water and moisture from the whole apparatus. After closing the valve at the outcome of the IR cell and collecting an IR background, the TPD run is started heating up the mixture at 5 °C/min up to 500 °C, collecting IR spectra every 20 °C. During the whole TPD run, the volatile products are accumulated in the IR cell, and at the end the reactor is cooled down to room temperature for the acquisition of the final IR spectrum.

TPD-IR experiments were complemented by gas chromatography-mass spectrometry (GC-MS). A small fraction of the volatile products was sampled from the IR cell with a syringe and then analysed by GC-MS, using an Agilent gas chromatograph mod 6890 plus equipped with a Varian VA-5MS column (30 m of length and 0.25 mm of internal diameter) and an Agilent mass spectrometer mod 5973 N. A sample volume of 1 µL was injected in the chromatographic column, purged with He flow (1 mL/min), and heated up from 35 °C to 500 °C with a heating ramp of 5 °C/min.

3. RESULTS AND DISCUSSION

3.1. Characterization of the catalytic materials

3.1.1. Structure and morphology of the mesoporous silicas

The synthetized mesoporous silicas were preliminary investigated to verify their structural properties in comparison to the literature. The low-angle PXRD patterns (Figure 1) confirm the formation of ordered mesopores in all the synthetized silicas. In particular, the patterns of the SBA-15 samples (Figure 1a) display a well resolved diffraction peak at around 0.9° corresponding to the (100) reflection, together with other less intense peaks at 1.5° and 1.8°, corresponding to the (110) and (200) reflections, respectively. These signals are typical of the p6mm hexagonal symmetry of the SBA-15 framework [33]. Compared to the pure SBA-15, the metal-substituted samples display reflections at lower 2θ values, more evident for Al-SBA-15 than for Zr-SBA-15. This shift corresponds to an increased d-spacing, which in turn indicates a larger unit cell (associable to larger mesopores). The d-spacing calculated applying the Bragg law to the (100) reflection are: 9.49 nm for SBA-15, 9.65 nm for Zr-SBA-15 and 10.62 nm for Al-SBA-15, which are consistent with expectation [35,36].

For what concerns the SBA-16 materials, the diffraction patterns (Figure 1b) display only the first diffraction peak at 0.8°, corresponding to the (110) reflection. The absence of a peak at ca. 1.3°, corresponding to the (200) reflection of the Im3m cubic structure of SBA-16, indicates that these samples have a less ordered structure compared to those reported in the literature [23,34]. Also in this case, the metal-substituted samples exhibit peaks slightly shifted towards lower angles compared to the pure SBA-16. The calculated d-spacings are respectively 9.83 nm for SBA-16 and 11.81 nm for both Al-SBA-16 and Zr-SBA-16. Again, this is suggesting that the introduction of Zr and Al in the silica framework leads to an increase of the pore dimension and thus enlarges the cell parameter.

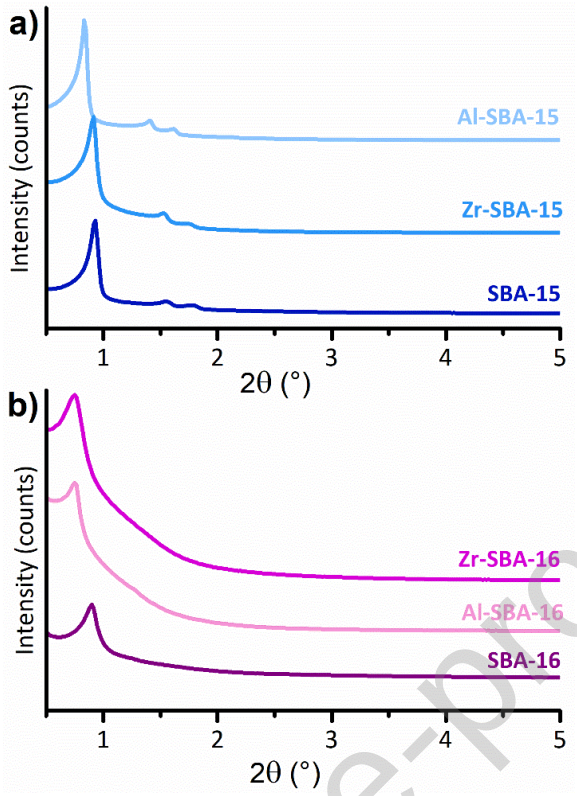

Figure 1. Low-angles PXRD patterns of the six mesoporous silicas synthetized in this work. Part a) refers to the SBA-15 materials, part b) to the SBA-16 ones.

FE-SEM and TEM microscopies were used to investigate the particles morphology and the order of the mesopores, respectively. Some representative images of SBA-15 and SBA-16 are shown in Figure 2, while similar images for all the other samples are displayed in Figures S1 and S2. SBA-15 (Figure 2a) displays a rod-like morphology with a well-ordered hexagonal array of mesopores (Figure 2b). Similar arrays are displayed by both Zr-SBA-15 and Al-SBA-15 (Figure S1d and FigureS1f), although with bigger pore dimensions, in agreement with the PXRD results. However, both Zr and Al-substituted samples exhibit diverse particles morphologies (Figure S1c and FigureS1e). In particular, both FE-SEM and TEM images (Figure S1c and Figure S3c) display that Zr-SBA-15 is clearly constituted by aggregations of platelet-like particles: this phenomenon has been already reported in the literature and explained in terms of a faster rate of silicate condensation on the micelles during the synthesis, induced by the presence of Zr^{4+} ions in the reaction mixture [35]. Al-substituted SBA-15 particles exhibit instead a larger and aggregated morphology, as confirmed by TEM images at low magnification (Figure S3a and FigureS3c).

On the other hand, pure SBA-16 is constituted by aggregated particles (Figure 2c) with a well-evident highly ordered cubic pore structure (Figure 2d) [34,44]. Both Zr-SBA-16 and Al-SBA-16 (Figure S2c-f) display similar morphology and porosity, although not homogeneously distributed

throughout the whole material, but alternating with some amorphous regions. The metals have been homogeneously substituted inside the mesoporous silica framework as underlined by the EDX elemental mapping (Figure S4a-d) acquired at different magnifications, and moreover the absence of extra-framework Zr or Al oxide phases is confirmed by the high-angle PXRD patterns (Figure S5a and Figure S5b) showing the long-range amorphous profile typical of this kind of materials.

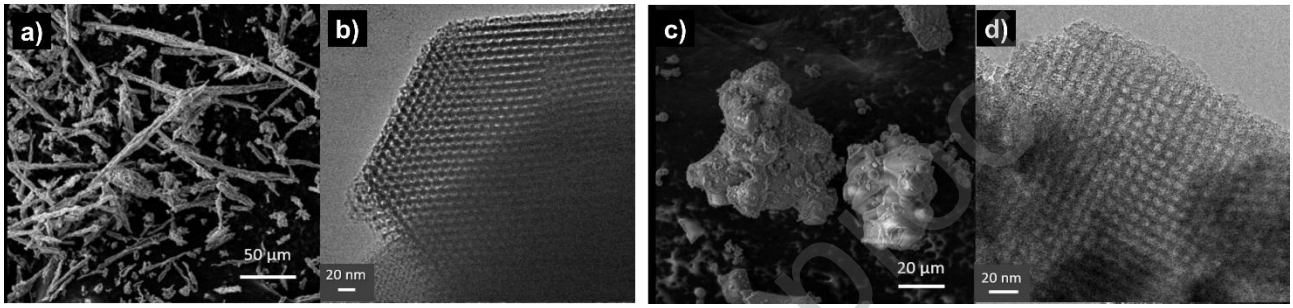

Figure 2. Parts a) and b) Representative FE-SEM and TEM images of SBA-15. Parts c) and d) The same for SBA-16.

3.1.2. Textural properties of the mesoporous silicas

The textural properties of the six synthetized mesoporous silicas were investigated by N_2 adsorption-desorption isotherms at 77 K. The isotherms of SBA-15 and SBA-16 are reported in Figure 3a and Figure 3b respectively, whereas all the others are reported in Figure S6c-f. According to IUPAC classification [45], all the isotherms can be described as intermediate between type I isotherms (typical of microporous materials) and type IV isotherms (displaying the hysteresis loop, typical of mesoporous materials). The region at low relative pressures indicates a high N_2 uptake due to the presence of micropores, which interconnect the mesoporous channels in SBA-15 materials and the spherical cages in SBA-16 materials. Finally, at higher relative pressures the isotherms are characterized by multilayer N_2 adsorption that occurs on the external surface of the materials. Two types of hysteresis loops can be distinguished: namely, H1 for SBA-15 sample, due to channel-like homogeneous open pores, and H2(a) for SBA-16, typical of bottle-neck, i.e., cage-like, mesopores. In the latter case, the desorption is characterized by a steeper decrease in the adsorbed quantity, because the bottle-neck obstructs the release of the trapped molecules, giving rise to cavitation effects [46].

By comparing the materials with the same framework, it is evident that the insertion of metals in the siliceous structure affects the shape of N_2 isotherms. For SBA-15 samples (see Figure S6, sections a-c-e), the step of the isotherm at low relative pressures due to the presence of

micropores interconnecting the main mesoporous cavities is basically the same in the pristine material and in the Zr-SBA-15, whereas it drastically decreases for Al-SBA-15, testifying a partial occlusion/disappearance of the micropores. The H1 hysteresis loop of SBA-15 is retained also in metal substituted silica, proving the size and shape homogeneity of the mesoporous channels. However, in both Zr-SBA-15 and Al-SBA-15 it has shifted to higher relative pressures due to the larger size of mesopores induced by the insertion of the metals in the framework, also confirmed by TEM micrographs of Figure S1. Still, the step generated by the capillary condensation in the silica channels, for both Zr- and Al- modified SBA-15, is definitely higher compared to reference SBA-15, testifying the availability of a larger pore volume. Concerning SBA-16 materials (See Figure S6, sections b-d-f), only the insertion of Al in the framework causes a reduction of the micropores as already observed in modified SBA-15 silica. Zr-SBA-16 and Al-SBA-16 exhibit the hysteresis loops at higher relative pressure compared to reference SBA-16, due to the enlargement of the mesoporous cages that is more evident for the Al-substituted sample. Moreover, the hysteresis loop shape changes for Zr-SBA-16 and Al-SBA-16 compared to pristine SBA-16, being now classified as type H2(b). This modification is probably generated by a different ratio between the size of the mesoporous cavity and the size of the cage entrance typical of the SBA-16 framework [46]. Finally, also for metal substituted SBA-16 the capillary condensation step is higher due to an enhanced volume of the spherical cages.

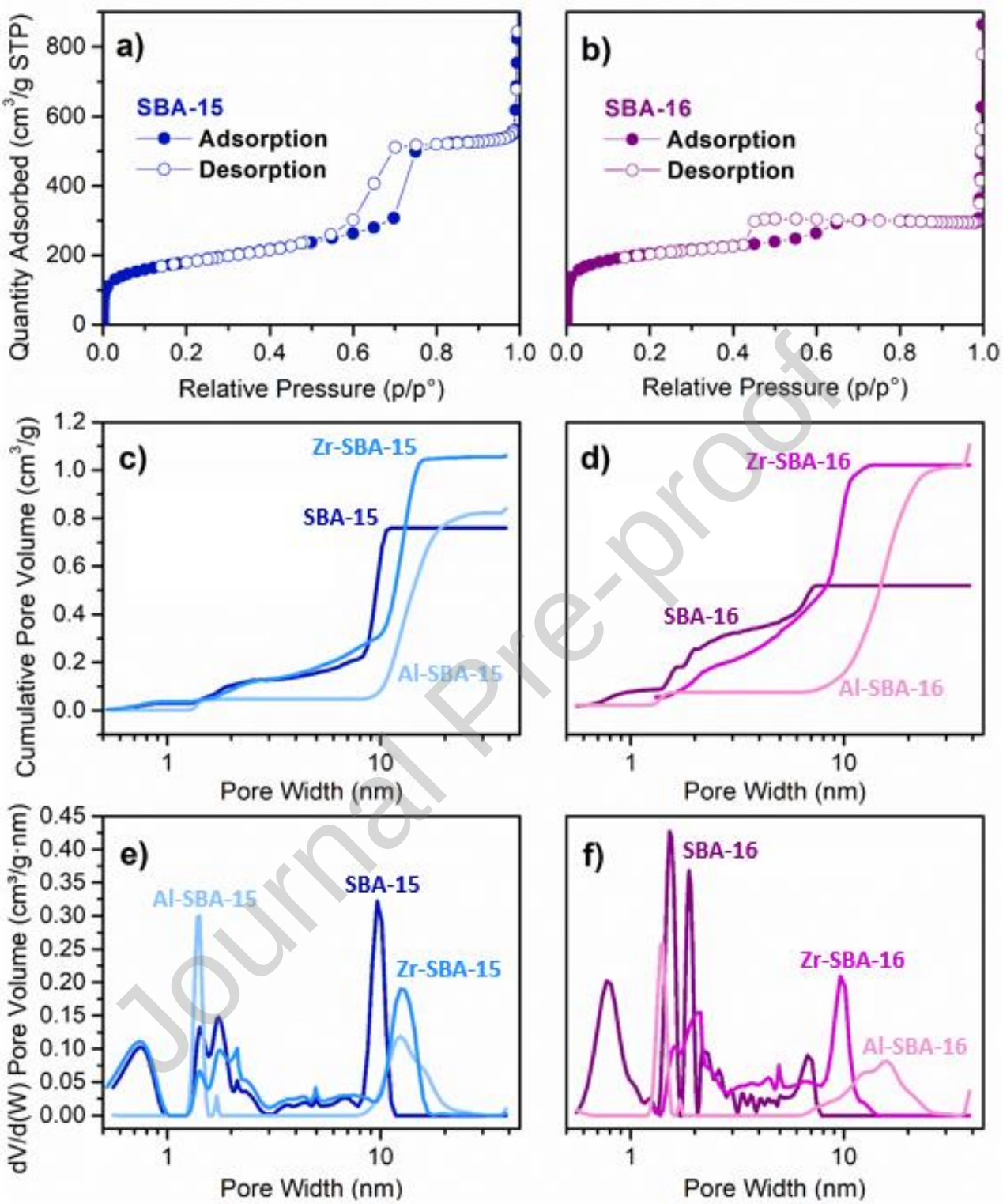

Figure 3. Parts a) and b) N_2 adsorption-desorption isotherms at 77 K for SBA-15 and SBA-16, respectively. Full and empty symbols refer to the adsorption and desorption branches respectively. Parts c) and d) Cumulative pore volume and parts e) and f) pore size distribution for the six mesoporous silicas obtained by using the NL-DFT method: sections c) and e) SBA-15, Zr-SBA-15, and Al-SBA-15, while sections d) and f) SBA-16, Zr-SBA-16, and Al-SBA-16.

N_2 adsorption-desorption isotherms have been analysed by using the BET equation to determine the SSA, as reported in Table 1. Pure mesoporous silicas and the Zr-substituted ones show values between 650-800 m^2/g, with the SBA-16 materials having SSAs slightly higher than

their SBA-15 counterparts, whereas the Al-substituted ones show smaller SSAs (around 400 m^2/g). These results are consistent with the literature [36,47,48]. Furthermore, the pore size distribution was determined by both the BJH (Figure S7c-d and Table S2) and the NL-DFT (Figure 3e-f and Table 1) methods. Even though the two methods gave similar results, the latter estimates both micropores and mesopores and it is more accurate in the description of bottle-neck pores. The NL-DFT pore size distribution of SBA-15 reported in Figure 3c exhibit a family of ordered mesopores at around 9 nm which shifts to higher pore size for both Zr- and Al-SBA-15 samples [23,34]. Different families of micropores interconnecting the main channels are well evident below 3 nm for all SBA-15 samples, though less numerous for the Al-containing silica. The SBA-16 materials present a more complex pore size distribution (Figure 3d) due to the presence of different mesopores families, the spherical cages and their entrance, with a smaller size. Both pure SBA-16 and Zr-SBA-16 exhibit a bimodal distribution of narrow mesopores between 1.5 and 2 nm, ascribable to two different cage openings. Al-SBA-15 has instead a single peak related to the mesopores entrance with a size of around 1.5 nm. Concerning the main cages, their size increases following this trend SBA-16 < Zr-SBA-16 < Al-SBA-16, as already pointed out by the position of the capillary condensation step in the isotherms [23,34]. Moreover, the cage size distribution of A-SBA-16 is broader and less defined compared to pure SBA-16 and Zr-SBA-16, highlighting a slight size heterogeneity of the cages, induced by the insertion of Al ions in the framework. Table 1 reports a summary of all the materials textural properties (BET SSA, pore size distribution and pore volume). In conclusion, for all samples, the insertion of a metal (either Al or Zr) in the siliceous framework increases the size of the mesopores, in good agreement with the increase in the unit cell parameter as detected by PXRD (Figure 1). This explains why the metal-substituted silicas are characterized by a total pore volume higher than pure mesoporous silicas. ~~Comparing the two silica frameworks, SBA-16 samples present a more complex pore size distribution than SBA-15 materials~~. Concerning instead the micropores, Al-substituted samples display an extremely low micropore volume with a quite sharp pore size distribution, that is reasonably the cause for their smaller SSA. On the contrary, both pure silicas and Zr-substituted samples present multiple pore size distributions of micropores, accounting on average for one third of the total pore volume.

Table 1. Specific Surface Area as determined by the BET equation (SSA_{BET}) and porosity (determined by the NL-DFT method) for the six synthetized mesoporous silicas. For the SBA-16 samples, the entrance of the cage mesopores is also reported.

Catalyst	SSA_{BET} (m^2/g)	V total (cm^3/g)	V micro (cm^3/g)	V meso (cm^3/g)	Mesopores size (nm)	Cage entrance (nm)

SBA-15	653 ± 2	0.76	0.20	0.56	9.8	-
Zr-SBA-15	726 ± 2	1.06	0.25	0.81	13.1	-
Al-SBA-15	422 ± 1	0.82	0.06	0.76	12.3	-
SBA-16	756 ± 2	0.42	0.26	0.14	6.9	1.5/1.9
Zr-SBA-16	813 ± 3	0.85	0.28	0.57	9.8	1.6/2.0
Al-SBA-16	432 ± 1	0.85	0.05	0.80	15.7	1.4

3.1.3. Surface acidity

IR spectroscopy was used to investigate the surface species of the mesoporous silicas after dehydroxylation. The spectra of the pure SBA-15 materials are reported in Figure S12: the spectral profile is typical of an activated SiO_2, with a very sharp absorption band at 3747 cm^{-1} ascribed to isolated surface OH groups (silanols), the out-of-scale silica framework vibrations at values below 1300 cm^{-1} and their overtones and combination modes in the 2000-1600 cm^{-1} range [49]. The spectrum of Zr-SBA-15 shows a weak additional band at 3785 cm^{-1}, which is attributed to isolated terminal hydroxy groups bonded to Zr [50], whereas that of Al-SBA-15 displays a weak band at 3610 cm^{-1}, which is assigned to ν(OH) of the Si-OH-Al groups (as typically observed in zeolite-type acidic materials) [51]. All in all, the spectra of pure materials demonstrate the presence of standard silanols and of a small fraction of hydroxy groups directly bonded to the heteroatoms, but they cannot provide information about their acidic properties. Therefore, pyridine adsorption was performed to quantify the acidic sites, not only on the mesoporous silicas but also on the three reference catalysts. The representative outcome of a typical experiment is shown in Figure S13 for SBA-15. Upon exposure to pyridine vapour pressure at RT, the well-defined ν(OH) band of isolated OH groups is consumed and converted into a very broad absorption band at lower wavenumbers due to the formation of intermolecular H-bonds with pyridine molecules. At the same time, new absorption bands, ascribed to the vibrational modes of adsorbed pyridine, appear in the 3100-3000 cm^{-1} and 1700-1400 cm^{-1} spectral regions [52]. These components are mostly stable upon degassing at RT under dynamic vacuum, indicating that pyridine is strongly adsorbed.

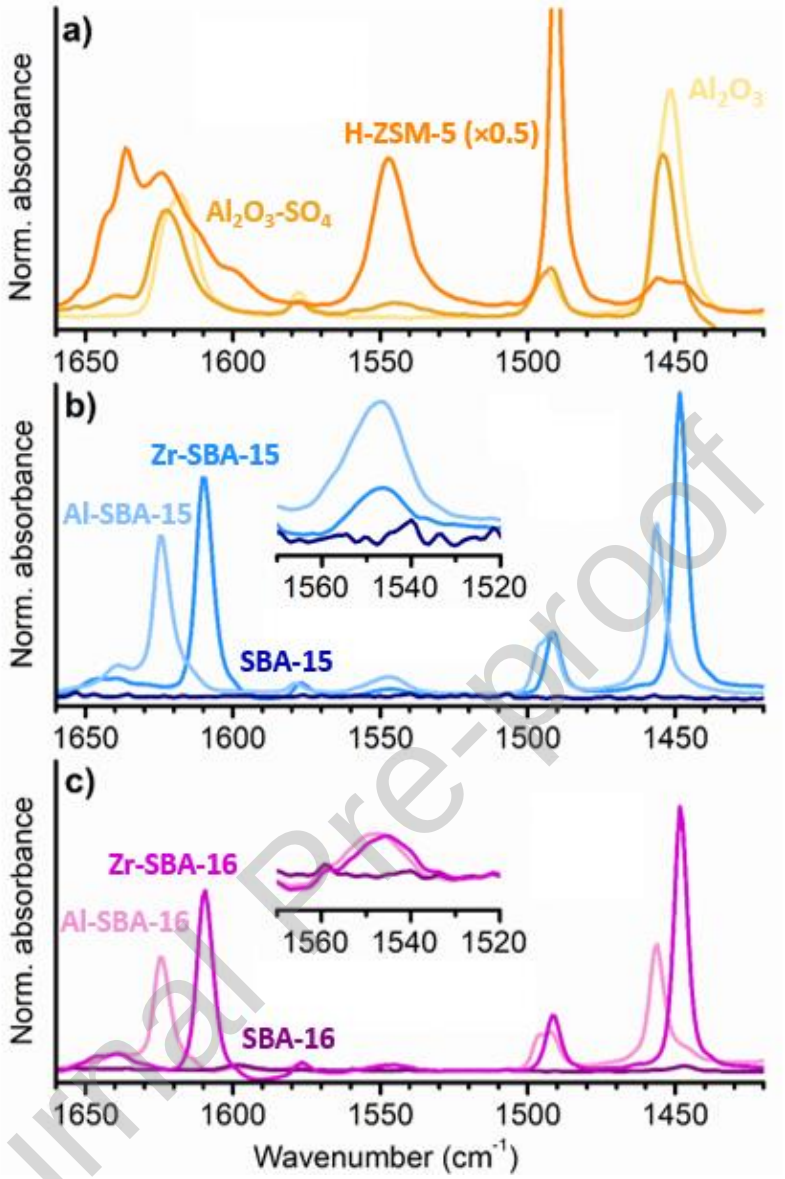

Figure 4. Part a) IR spectra of pyridine chemisorbed on the three reference catalysts (obtained after contacting the samples with pyridine at RT and successively degassing at 200 °C for 1 h). The spectra are shown in the region between 1670 and 1420 cm^{-1}, after subtraction of the spectra collected prior pyridine dosage and normalized to the optical density of the pellet. Part b) and Part c) The same as Part a) for the catalysts with SBA-15 and SBA-16 topology, respectively. The inset shows a magnification of the band ascribed to pyridinium cations formed at the Bronsted acid sites.

Afterwards, the sample was outgassed at 200 °C for 1 h, to remove all the adsorbed pyridine except that chemisorbed at both Lewis (LAS) and Brønsted (BAS) surface acid sites. Figure 4 shows the IR spectra of pyridine chemisorbed on all the samples in the 1670-1420 cm^{-1} region, after subtraction of the spectra collected prior pyridine dosage and normalization to the optical density of the pellets. Four main bands are observed in all cases, differing in spectral position and

in their relative intensity. The most significant ones are those located at about 1450 cm^{-1}, attributed to the 19a vibrational mode of pyridine in interaction with LAS, and at 1545 cm^{-1}, attributed to pyridinium cation formed on BAS [52]. These two bands can be used to estimate the concentration of both BAS and LAS referred to the unit weight of each sample (i.e., in µmol/g) as reported elsewhere [53], knowing the molar extinction coefficients of the two bands, as measured by Emeis et al. [54].

Table 2 summarizes the overall results, reporting both the quantification of the LAS and BAS sites and the position of the LAS absorption band compared to the frequency of unperturbed pyridine ($\Delta\nu_{LAS}$), which is indicative of the acid strength (i.e., the larger the shift, the stronger the acidity). Concerning the reference catalysts (Figure 4a), alumina does not contain BAS sites, but only a substantial amount (249 µmol/g) of medium acidic LAS ($\Delta\nu_{LAS}$ = +11 cm^{-1}). The sulphation process induces the formation of BAS (29 µmol/g), at the expenses of the concentration of LAS (165 µmol/g), which however become slightly more acidic ($\Delta\nu_{LAS}$ = +14 cm^{-1}). Instead, H-ZSM-5 presents a very large amount of BAS (671 µmol/g, almost twenty times higher than sulphated alumina), despite a modest amount of LAS (60 µmol/g), divided in two distinct families (with weak and medium acidity).

Table 2. Summary of the acid properties and effect of each catalyst on the LLDPE degradation temperatures. C_{BAS} and C_{LAS}: concentration of Brønsted and Lewis acid sites; $\Delta\nu_{LAS}$: position (in cm^{-1}) of the two IR absorption bands characteristic for pyridine adsorbed at Lewis acid sites (LAS) with respect to the position of the corresponding band in the IR spectrum of neat pyridine (ν_{LAS} = 1440 cm^{-1}); T_{start} and T_{max}: starting temperature and temperature at which the rate of catalytic degradation of LLDPE is maximum. The thermal degradation of LLDPE in absence of any catalyst is characterized by T_{start}= 429 °C and T_{max}= 454 °C.

	CATALYSTS ACIDITY			**LLDPE DEGRADATION**	
CATALYST	**C_{BAS} (µmol/g)**	**C_{LAS} (µmol/g)**	**$\Delta\nu_{LAS}$ (cm^{-1})**	**T_{start} (°C)**	**T_{max} (°C)**
Al_2O_3	-	248.55	+11	424	450
Al_2O_3-SO_4	29.42	164.82	+14	276	383
H-ZSM-5	671.34	59.62	+8, +14	342	380
SBA-15	-	-	-	424	454
Zr-SBA-15	7.76	140.77	+8	394	437
Al-SBA-15	23.61	96.49	+17	355	387
SBA-16	-	2.53	+6	429	463
Zr-SBA-16	9.49	123.87	+8	389	425
Al-SBA-16	9.01	60.95	+17	370	397

Moving to mesoporous silicas (Figure 4b and Figure 4c), while the pure ones display almost no acidity, the metal insertion induces the formation of both LAS and BAS sites. In particular, the

Zr-substituted samples present the highest content of LAS (around 124-140 μmol/g), although the small $\Delta\nu_{LAS}$ (+8 cm^{-1}) suggests a quite modest acid strength. In contrast, LASs on the Al-substituted samples are less (around 60-96 μmol/g), but stronger ($\Delta\nu_{LAS}$ = +17 cm^{-1}). Furthermore, Al-SBA-15 also displays a significant amount of BAS (23 μmol/g), whereas the BASs on Al-SBA-16 are in the same range as for the Zr-substituted samples (around 9 μmol/g).

3.2. Thermo-catalytic upcycling of LLDPE

3.2.1. Catalysts effects on the ~~thermodynamic~~ kinetics of the LLDPE degradation process

At first, the catalytic degradation of LLDPE was monitored by TGA. Figure 5a shows the LLDPE degradation conversion X_{LLDPE} defined as $(W_0–W_T)/W_0$ x 100, where W_0 is the initial LLDPE weight and W_T is the weight of LLDPE at a given temperature. These data allow evaluating the temperature at which the decomposition reaction starts (T_{start}, defined as the temperature at which X_{LLDPE} = 5%) and the temperature at which the rate of the reaction is maximum (T_{max}, evaluated as the maximum of the derivative curve): they are summarized in Figure 5b and in Table 2 (last two columns). In the absence of any catalyst, the thermal degradation of LLDPE starts at a temperature around 429 °C, with a maximum reaction rate at 454 °C; above 500 °C the polymer is completely decomposed, and no further reaction takes place. The presence of Al_2O_3 does not significantly affect the degradation temperature, while both Al_2O_3-SO_4 and H-ZSM-5 substantially decrease the LLDPE degradation temperature, with T_{max} around 380 °C. It is worth noting that Al_2O_3-SO_4 shows a much lower T_{start} value than H-ZSM-5, likely because the active sites are immediately available for interacting with the polymer chains, without any diffusion limitation.

Pure mesoporous silicas (SBA-15 and SBA-16) have almost no influence on the thermal profile of LLDPE degradation. The metal-substituted mesoporous silicas, instead, affect both T_{start} and T_{max}. The two Al-containing samples display the largest effect, with T_{max} almost approaching those obtained in the presence of Al_2O_3-SO_4 and H-ZSM-5. The two Zr-containing samples, instead, display an intermediate behavior (T_{max} at 437 and 425 °C for Zr-SBA-15 and Zr-SBA-16 respectively), despite the higher amount of LAS and a similar amount of BAS. Clearly, not only the amount of acid sites plays a role in LLDPE degradation, but also their acidic strength (vide infra).

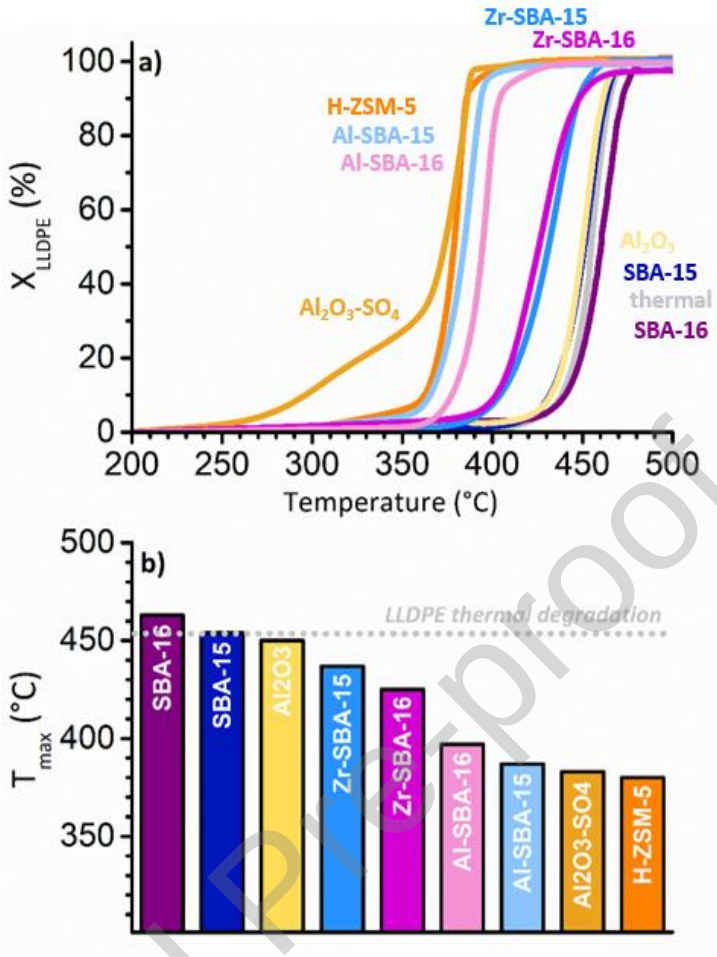

Figure 5. Part a): Conversion of LLDPE as a function of temperature in the presence of different catalysts (in a 1:1 ratio), as obtained from TGA data. $X_{LLDPE}= (W_0–W_T)/W_0$ x 100 where W_0 is the initial LLDPE weight and W_T is the weight of LLDPE at a given temperature T. Part b): Temperature at which the rate of the reaction is maximum (T_{max}), evaluated as the maximum of the first derivative of the TGA curves reported in part a.

3.2.2. Catalysts effects on the selectivity of the LLDPE degradation process

Beside influencing the kinetics ~~thermodynamic~~ of the LLDPE degradation, the catalyst has important consequences on the selectivity of the process. To investigate this aspect, we have developed a TPD-IR set-up (complemented by GC-MS) for identifying and quantifying the volatile reaction products. Our own TPD-IR experimental set-up is very simple, versatile, and achievable by standard lab equipment. Even though it operates in accumulation, low partial pressures are achieved in the cell, which minimizes the occurrence of secondary reactions. Moreover, it allows the identification of the IR active gases released at high concentration as well as of those produced at traces, as recently demonstrated by some of us [41].

At first, during a typical LLDPE upcycling experiment a fraction of the volatile products accumulated in the IR cell was sampled and sent to the GC-MS instrument (Figure S14 and Table S2). The identified species mainly comprise a mixture of light gases with short chain (in the C2-C4

range) and some heavier molecules with longer chain (composed mainly of C5 and C6). A high portion of the mixture is attributed to a series of branched products, all containing a double bond in position 1 and a methyl group in position 2. This distribution is similar to that reported in the literature, in terms of carbon number [36,55], but in our case no cyclic nor aromatic hydrocarbons are detected.

Successively, the on-line quantification of the volatile products was performed by IR spectroscopy. A representative IR spectrum collected at the end of a LLDPE upcycling experiment is shown in Figure S15a. It is quite complex since it contains the spectroscopic signatures of the accumulated multiple gases. The spectra collected during the temperature ramp were all the same, except for the total intensity, indicating that all the volatile products are evolved simultaneously. For this reason, only the IR spectrum collected at the end of the experiment was used for quantification. The comparison with the spectra of reference compounds (Figure S15b) allowed the assignment of the main absorption bands to specific volatile products and/or to families of products. For example, methane, propylene, and butane were clearly recognizable when present, while the IR spectra of branched products (2-methyl-1-propene, 2-methyl-1-butene and 2-methyl-1-pentene) are very similar to each other, so that they were grouped in the family labeled as "C4-C6 branch". For the quantification, a characteristic band was chosen for each compound or class of compounds (Table S3) and a calibration curve was built up to correlate the intensity of the chosen band to the pressure and thus to the quantity of the corresponding compound, by using the ideal gas law. A few products recognized with GC-MS (e.g., 2-methylpropane, 2-butene and 1-pentene), which however constitute only a minor fraction of the whole chromatogram, were not quantifiable by means of IR spectroscopy because it was not possible to select for them a sufficiently isolated characteristic band.

Figure 6 shows a summary of the main results, in terms of grams of volatile products per grams of LLDPE. The catalysts are ordered according to their T_{max} value as determined by TGA (Figure 5b). In absence of any catalyst (i.e., LLDPE thermal degradation) very low amounts of volatile products are obtained (less than 5 %), with a very heterogeneous composition. Indeed, most of the polymer is degraded to waxes and/or heavy compounds, which stick on the walls of the reactor without reaching the IR cell. Roughly the same amounts of volatile products were obtained in the presence of SBA-16, SBA-15 and Al_2O_3, confirming that they are almost ineffective for this reaction, in good agreement with the negligible variation of T_{max} as determined by TGA results. In presence of Zr-SBA-15 and Zr-SBA-16 the fraction of volatile products remains low, but

their distribution is narrowed. In particular, butane is no more observed, and a higher quantity of branched products is obtained with Zr-SBA-16.

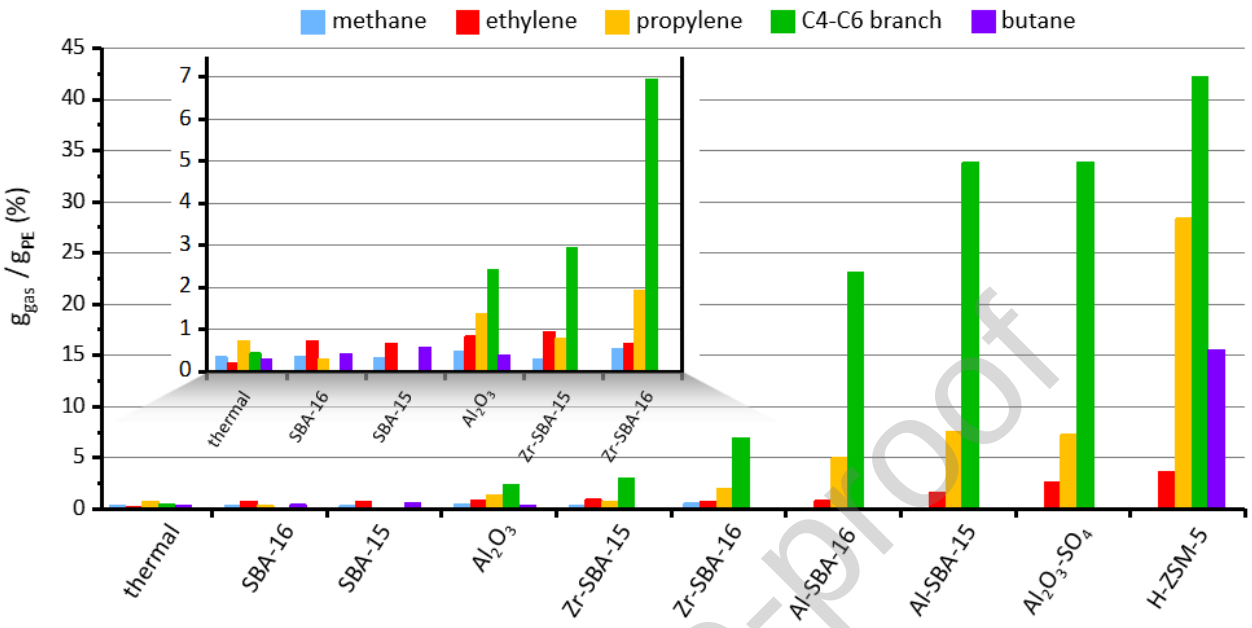

Figure 6. Quantification of the volatile products evolved during the catalytic upcycling of LLDPE in the presence of different catalysts. The quantities are expressed in grams of volatile products per grams of LLDPE. The results of LLDPE thermal degradation (i.e., in the absence of any catalyst) are also reported for comparison. The catalysts are ordered according to their T_{max} value as determined by TGA (Figure 5b).

A much larger fraction of volatile products is obtained in the presence of Al-SBA-16 and, especially, Al-SBA-15. Moreover, methane is not produced at all with these catalysts, and a steep increase in the quantity of propylene (about 5-7.5 %) and branched products (almost 25-35%) is observed. The performances of Al-SBA-15 are very similar to those of Al_2O_3-SO_4. Finally, H-ZSM-5 leads to the highest amount of volatiles, but with a broader distribution and a substantial amount of butane.

It is worth remarking that the quantification was done in the most conservative way as possible, quantifying only the species that were univocally determined by IR, so that some gases products were not evaluated (such as the minor fractions of linear alkanes and alkenes detected by GC-MS), despite contributing to the overall mass balance. Finally, the solid residues were measured to complete the mass balance compared to the original mass of the polymer: almost negligible in the cases of H-ZSM-5, Al_2O_3-SO_4 and Al-substituted silicas (about 5%), visibly predominant in all the other cases (above 90%).

3.2.3. Catalysts stability

Finally, the stability of the two most interesting catalysts, namely Al-SBA-15 and Al_2O_3-SO_4, was investigated. The catalysts were recovered at the end of the LLDPE degradation, reactivated by calcination in air at 500 °C and employed again in successive LLDPE degradation cycles (Figure 7). For Al_2O_3-SO_4 (Figure 7a), the total yield of volatile products drastically drops during the second run (just 7.5%), approaching the outcome of LLDPE degradation with pure Al_2O_3. Reasonably this behavior is due to the leaching of the sulphate species by reaction with the polymer chains during the first LLDPE degradation cycle. For Al-SBA-15, instead, only a modest decrease of the catalytic activity is observed during the second cycle (the total fraction of volatile products decreases from 43 % to 34 %). Nevertheless, both the activity and the selectivity remain stable along the next cycles of regeneration and reuse. This suggests that a small fraction of active sites is irreversibly poisoned during the first LLDPE degradation process, while all the others can be effectively restored upon each regeneration.

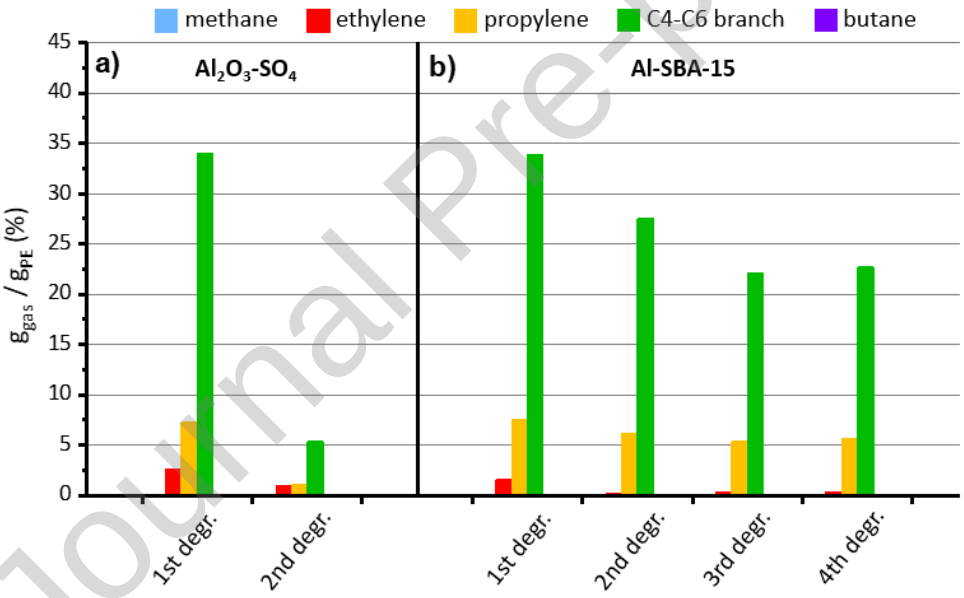

Figure 7. Part a) Quantification of the volatile products obtained during the first catalytic upcycle of LLDPE in the presence of Al_2O_3-SO_4 (part s) and Al-SBA-15 (part b), and during successive cycles, after regenerating the catalyst by calcination in air at 500 °C.

3.3. Correlation between the properties of catalysts and their performances

The data collected in this work allowed us to rationalize, at least in part, the effects of different catalyst properties on their performance in the catalytic pyrolysis of POs. In general terms, the amount of volatile products obtained at the end of the LLDPE pyrolysis was found to correlate with T_{max}, the temperature at which the rate of catalytic degradation is maximum: this means that the catalysts exhibiting the highest influence on the kinetics ~~thermodynamic~~ of the process, are also those giving the highest volatile products yield. Hence, T_{max} can be used to

roughly estimate the efficiency of similar catalysts in the upcycling of POs. Moreover, the efficiency of the catalysts is driven more by the acidity than by the porous structure. The presence of pores does not influence the yield of volatile products. However, comparing the activity in PE degradation of non-porous Al_2O_3 and Zr-substituted mesoporous silicas having a similar acidity, we can conclude that in the presence of mesopores the PE degradation temperature is lowered. This is likely due to the concentration of the polymer within the pores, which improves the heat transfer.

Figure 8 correlates T_{max} with the concentration of BAS and LAS sites, and with the strength of the latter. A very good correlation is found in the case of Brønsted acid sites (Figure ~~9~~8a): the higher the amount of BAS, the lower T_{max}, in good agreement with the literature [56,57], although with some exceptions. In particular, H-ZSM-5 stands as an outlier in terms of number of BAS sites, but its T_{max} is similar to the one found for the two Al-substituted silicas, which contain twenty times less BAS sites. This suggests that BAS sites play a pivotal role in lowering the LLDPE degradation temperature, but only up to a certain limit. Interestingly, even though H-ZSM-5 is the catalyst with the highest volatiles yield, it is less selective than the Al-substituted silicas since it produces a substantial amount of butane. This suggests that too many BAS sites hosted in a microporous framework negatively affect the selectivity, likely promoting secondary reaction paths which are not favored on less acidic catalysts.

In contrast, almost no correlation was found among T_{max} and the amount of LAS (Figure ~~9~~8b): Al-substituted mesoporous silicas have a relatively small amount of LAS, but show T_{max} lower than 400 °C, while Zr-substituted silicas have a larger amount of LAS, but a higher T_{max}. A better correlation is found between T_{max} and the strength of LAS (Figure ~~9~~8c): the stronger the LAS, the lower T_{max}, irrespectively of their amount.

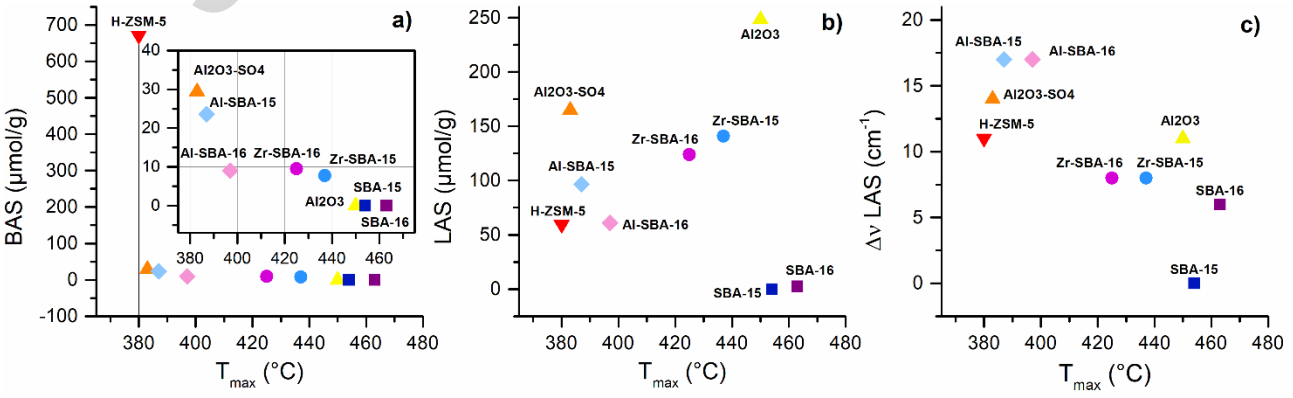

Figure 8. Correlation between the amount of Brønsted (part a), Lewis (part b) acid sites of the catalysts, and $\Delta\nu_{LAS}$ (part c) and the T_{max} of LLDPE degradation.

4. CONCLUSIONS

In this work, six different mesoporous silicas were synthetized, based on either SBA-15 or SBA-16 structures, either pure or substituted with metals. In particular, Al was chosen to introduce surface acidic species, while Zr was chosen to enlarge the dimension of the pores by forming larger micelles of organic template during the hydrothermal synthesis and to modify the particles morphology from rod-like to platelets by accelerating TEOS condensation around the micelles. In this way it was possible to systematically investigate the structural and chemical properties, isolating the effect of each parameter on the overall behavior.

These materials were tested in the catalytic pyrolysis of LLDPE, comparing the obtained results with the thermal pyrolysis and with the catalytic pyrolysis in the presence of reference materials. The activity of the catalysts was evaluated considering both the temperature dependence of the process and the selectivity towards volatile products. In general, there is a quite good correlation between those two aspects: the catalyst with the highest yield is also the catalyst that most lowers the reaction temperature. This fact represents a great advantage in the perspective of scaling up the process, allowing a higher chemical conversion with a lower energy demand.

All in all, this study demonstrates that solid acid catalysts are beneficial in improving the pyrolysis of POs, constituting a very versatile system, whose chemical and structural properties can be finely customized. BAS sites seem fundamental but exceeding in their concentration leads to a loss in selectivity. Mesoporous silica catalysts containing a well-balanced amount of BAS and strong LAS sites represent a good compromise for optimizing activity and selectivity and moreover, the distribution of the active sites inside an ordered system of mesoporous channels helps in maintaining good catalytic performances upon cyclic experiments, a key feature for any catalyst.

REFERENCES

[1] I. Vollmer, M.J.F. Jenks, M.C.P. Roelands, R.J. White, T. van Harmelen, P. de Wild, G.P. van der Laan, F. Meirer, J.T.F. Keurentjes, B.M. Weckhuysen, Beyond Mechanical Recycling: Giving New Life to Plastic Waste, Angewandte Chemie - International Edition. 59 (2020) 15402–15423. https://doi.org/10.1002/anie.201915651.

[2] Plastics Europe, Plastics - the Facts 2022, (2022). https://plasticseurope.org/knowledge-hub/plastics-the-facts-2022/ (accessed December 7, 2022).

[3] World Economic Forum, Ellen McArthur Foundation and McKinsey & Company, The New Plastics Economy: Rethinking the Future of Plastics & Catalysing Action, 2017.

[4] R. Geyer, J.R. Jambeck, K.L. Law, Production, use, and fate of all plastics ever made, Sci Adv. (2017). https://www.science.org.

[5] J.R. Jambeck, R. Geyer, C. Wilcox, T.R. Siegler, M. Perryman, A. Andrady, R. Narayan, K.L. Law, Plastic waste inputs from land into the ocean, Science (1979). 347 (2015) 768–771. https://doi.org/10.1126/science.1260352.

[6] M. de Smet, M. Linder, Maurizio. Crippa, Bruno. De Wilde, Rudy. Koopmans, Jan. Leyssens, Jane. Muncke, A.-Christine. Ritschkoff, K. van. Doorsselaer, Costas. Velis, Martin. Wagner, European Commission. Directorate-General for Research and Innovation., A circular economy for plastics : insights from research and innovation to inform policy and funding decisions, 2019.

[7] A. Piovano, E. Paone, The reductive catalytic upcycling of polyolefin plastic waste, Current Research in Green and Sustainable Chemistry. 5 (2022). https://doi.org/10.1016/j.crgsc.2022.100334.

[8] X. Chen, Y. Wang, L. Zhang, Recent Progress in the Chemical Upcycling of Plastic Wastes, ChemSusChem. 14 (2021) 4137–4151. https://doi.org/10.1002/cssc.202100868.

[9] P.A. Kots, B.C. Vance, D.G. Vlachos, Polyolefin plastic waste hydroconversion to fuels, lubricants, and waxes: A comparative study, React Chem Eng. 7 (2022) 41–54. https://doi.org/10.1039/d1re00447f.

[10] C. Wang, H. Han, Y. Wu, D. Astruc, Nanocatalyzed upcycling of the plastic wastes for a circular economy, Coord Chem Rev. 458 (2022). https://doi.org/10.1016/j.ccr.2022.214422.

[11] J. Huang, A. Veksha, W.P. Chan, A. Giannis, G. Lisak, Chemical recycling of plastic waste for sustainable material management: A prospective review on catalysts and processes, Renewable and Sustainable Energy Reviews. 154 (2022). https://doi.org/10.1016/j.rser.2021.111866.

[12] N.M. Wang, G. Strong, V. DaSilva, L. Gao, R. Huacuja, I.A. Konstantinov, M.S. Rosen, A.J. Nett, S. Ewart, R. Geyer, S.L. Scott, D. Guironnet, Chemical Recycling of Polyethylene by Tandem Catalytic Conversion to Propylene, J Am Chem Soc. (2022). https://doi.org/10.1021/jacs.2c07781.

[13] K. Ragaert, L. Delva, K. Van Geem, Mechanical and chemical recycling of solid plastic waste, Waste Management. 69 (2017) 24–58. https://doi.org/10.1016/j.wasman.2017.07.044.

[14] P.T. Williams, E.A. Williams, Fluidised bed pyrolysis of low density polyethylene to produce petrochemical feedstock, 1999.

[15] L. Dai, N. Zhou, K. Cobb, P. Chen, Y. Wang, Y. Liu, R. Zou, H. Lei, B.A. Mohamed, Y. Cheng, R. Ruan, Insights into structure–performance relationship in the catalytic cracking of high density polyethylene, Appl Catal B. 318 (2022). https://doi.org/10.1016/j.apcatb.2022.121835.

[16] A.J. Martín, C. Mondelli, S.D. Jaydev, J. Pérez-Ramírez, Catalytic processing of plastic waste on the rise, Chem. 7 (2021) 1487–1533. https://doi.org/10.1016/j.chempr.2020.12.006.

[17] H. Zhou, Y. Wang, Y. Ren, Z. Li, X. Kong, M. Shao, H. Duan, Plastic Waste Valorization by Leveraging Multidisciplinary Catalytic Technologies, ACS Catal. 12 (2022) 9307–9324. https://doi.org/10.1021/acscatal.2c02775.

[18] W. Kaminsky, F. Hartmann, New Pathways in Plastics Recycling, Angew Chem Int Ed Engl. 39 (2000) 331–333.

[19] Chevron Phillips Chemical, Chevron Phillips Chemical successfully completes first U.S. commercial scale production of circular polyethylene from recycled mixed-waste plastics., (2020). https://www.cpchem.com/media-events/news/press-release/chevron-phillips-chemical-successfully-completes-first-us (accessed December 7, 2022).

[20] SABIC, SABIC outlines intentions for Trucircle™ to close loop on plastic recycling. , (2020). https://www.sabic.com/en/news/21891-sabic-outlines-intentions-for-trucircle-to-close-loop-on-plastic-recycling (accessed December 7, 2022).

[21] BASF, ChemCycling™: from plastic waste to virgin-grade products, (2020). https://www.basf.com/global/en/who-we-are/sustainability/we-drive-sustainable-solutions/circular-economy/mass-balance-approach/chemcycling.html (accessed December 7, 2022).

[22] A.K. Panda, R.K. Singh, D.K. Mishra, Thermolysis of waste plastics to liquid fuelA suitable method for plastic waste management and manufacture of value added products—A world prospective, Renewable and Sustainable Energy Reviews. 14 (2010) 233–248. https://doi.org/10.1016/j.rser.2009.07.005.

[23] S.J. Choi, Y.K. Park, K.E. Jeong, T.W. Kim, H.J. Chae, S.H. Park, J.K. Jeon, S.S. Kim, Catalytic degradation of polyethylene over SBA-16, Korean Journal of Chemical Engineering. 27 (2010) 1446–1451. https://doi.org/10.1007/s11814-010-0281-9.

[24] D.K. Ratnasari, M.A. Nahil, P.T. Williams, Catalytic pyrolysis of waste plastics using staged catalysis for production of gasoline range hydrocarbon oils, J Anal Appl Pyrolysis. 124 (2017) 631–637. https://doi.org/10.1016/j.jaap.2016.12.027.

[25] P.N. Sharratt, Y.-H. Lin, A.A. Garforth, J. Dwyer, Investigation of the Catalytic Pyrolysis of High-Density Polyethylene over a HZSM-5 Catalyst in a Laboratory Fluidized-Bed Reactor, Ind Eng Chem Res. (1997). https://pubs.acs.org/sharingguidelines.

[26] Y.H. Lin, M.H. Yang, T.F. Yeh, M.D. Ger, Catalytic degradation of high density polyethylene over mesoporous and microporous catalysts in a fluidised-bed reactor, Polym Degrad Stab. 86 (2004) 121–128. https://doi.org/10.1016/j.polymdegradstab.2004.02.015.

[27] M. Artetxe, G. Lopez, M. Amutio, G. Elordi, J. Bilbao, M. Olazar, Cracking of high density polyethylene pyrolysis waxes on HZSM-5 catalysts of different acidity, Ind Eng Chem Res. 52 (2013) 10637–10645. https://doi.org/10.1021/ie4014869.

[28] J. Aguado, D.P. Serrano, G. San Miguel, M.C. Castro, S. Madrid, Feedstock recycling of polyethylene in a two-step thermo-catalytic reaction system, J Anal Appl Pyrolysis. 79 (2007) 415–423. https://doi.org/10.1016/j.jaap.2006.11.008.

[29] Y. Uemichi, M. Hattori, T. Itoh, J. Nakamura, M. Sugioka, Deactivation Behaviors of Zeolite and Silica-Alumina Catalysts in the Degradation of Polyethylene, Industrial Engineering Chemistry Research. (1998). https://pubs.acs.org/sharingguidelines.

[30] A. Marcilla, M.I. Beltrán, R. Navarro, Thermal and catalytic pyrolysis of polyethylene over HZSM5 and HUSY zeolites in a batch reactor under dynamic conditions, Appl Catal B. 86 (2009) 78–86. https://doi.org/10.1016/j.apcatb.2008.07.026.

[31] Y. Wang, Y. Zhang, H. Fan, P. Wu, M. Liu, X. Li, J. Yang, C. Liu, P. Bai, Z. Yan, Elucidating the structure-performance relationship of typical commercial zeolites in catalytic cracking of low-density polyethylene, Catal Today. (2022). https://doi.org/10.1016/j.cattod.2022.06.024.

[32] Nishu, R. Liu, M.M. Rahman, M. Sarker, M. Chai, C. Li, J. Cai, A review on the catalytic pyrolysis of biomass for the bio-oil production with ZSM-5: Focus on structure, Fuel Processing Technology. 199 (2020). https://doi.org/10.1016/j.fuproc.2019.106301.

[33] D. Zhao, J. Feng, Q. Huo, N. Melosh, G.H. Fredrickson, B.F. Chmelka, G.D. Stucky, Triblock Copolymer Syntheses of Mesoporous Silica with Periodic 50 to 300 Angstrom Pores, Science (1979). 279 (1998) 548–552. https://doi.org/10.1126/science.279.5350.548.

[34] R. Maheswari, V.V. Srinivasan, A. Ramanathan, M.P. Pachamuthu, R. Rajalakshmi, G. Imran, Preparation and characterization of mesostructured Zr-SBA-16: efficient Lewis acidic catalyst for Hantzsch reaction, Journal of Porous Materials. 22 (2015) 705–711. https://doi.org/10.1007/s10934-015-9943-7.

[35] S.Y. Chen, C.Y. Tang, W.T. Chuang, J.J. Lee, Y.L. Tsai, J.C. Chan, C.Y. Lin, Y.C. Liu, S. Cheng, A facile route to synthesizing functionalized mesoporous SBA-15 materials with platelet morphology and short mesochannels, Chemistry of Materials. 20 (2008) 3906–3916. https://doi.org/10.1021/cm703500c.

[36] Z. Zhang, K. Gora-Marek, J.S. Watson, J. Tian, M.R. Ryder, K.A. Tarach, L. López-Pérez, J. Martínez-Triguero, I. Melián-Cabrera, Recovering waste plastics using shape-selective nano-

scale reactors as catalysts, Nat Sustain. 2 (2019) 39–42. https://doi.org/10.1038/s41893-018-0195-9.

[37] J.M.R. Gallo, C. Bisio, L. Marchese, H.O. Pastore, One-pot synthesis of mesoporous [Al]-SBA-16 and acidity characterization by CO adsorption, Microporous and Mesoporous Materials. 145 (2011) 124–130. https://doi.org/10.1016/j.micromeso.2011.05.005.

[38] G.A.H. Mekhemer, H.A. Khalaf, S.A.A. Mansour, A.K.H. Nohman, Sulfated Alumina Catalysts: Consequences of Sulfate Content and Source, Monatshefte Für Chemie - Chemical Monthly. 136 (2005) 2007–2016. https://doi.org/10.1007/s00706-005-0374-z.

[39] J. Rouquerol, P. Llewellyn, F. Rouquerol, Is the bet equation applicable to microporous adsorbents?, in: Stud Surf Sci Catal, 2007: pp. 49–56. https://doi.org/10.1016/S0167-2991(07)80008-5.

[40] J. Hedlund, M. Zhou, A. Faisal, O.G.W. Öhrman, V. Finelli, M. Signorile, V. Crocellà, M. Grahn, Controlling diffusion resistance, selectivity and deactivation of ZSM-5 catalysts by crystal thickness and defects, J Catal. 410 (2022) 320–332. https://doi.org/10.1016/j.jcat.2022.04.013.

[41] E. Vottero, M. Carosso, R. Pellegrini, A. Piovano, E. Groppo, Assessing the functional groups in activated carbons through a multi-technique approach, Catal Sci Technol. 12 (2022) 1271–1288. https://doi.org/10.1039/d1cy01751a.

[42] R. Liu, W. Cai, X. Ni, L. Shi, R. Wang, S. Lin, Ultrastable and strongly acidic Al-SBA-15 with superior activity in LDPE catalytic cracking reaction, J Solid State Chem. 286 (2020) 121319. https://doi.org/10.1016/j.jssc.2020.121319.

[43] D.P. Serrano, J. Aguado, J.M. Escola, J.M. Rodríguez, L. Morselli, R. Orsi, Thermal and catalytic cracking of a LDPE-EVA copolymer mixture, J Anal Appl Pyrolysis. 68–69 (2003) 481–494. https://doi.org/10.1016/S0165-2370(03)00037-8.

[44] Z. Cao, P. Du, A. Duan, R. Guo, Z. Zhao, H. lei Zhang, P. Zheng, C. Xu, Z. Chen, Synthesis of mesoporous materials SBA-16 with different morphologies and their application in dibenzothiophene hydrodesulfurization, Chem Eng Sci. 155 (2016) 141–152. https://doi.org/10.1016/j.ces.2016.08.001.

[45] M. Thommes, K. Kaneko, A. V. Neimark, J.P. Olivier, F. Rodriguez-Reinoso, J. Rouquerol, K.S.W. Sing, Physisorption of gases, with special reference to the evaluation of surface area and pore size distribution (IUPAC Technical Report), Walter de Gruyter GmbH, 2015. https://doi.org/10.1515/pac-2014-1117.

[46] C. Schlumberger, M. Thommes, Characterization of Hierarchically Ordered Porous Materials by Physisorption and Mercury Porosimetry—A Tutorial Review, Adv Mater Interfaces. 8 (2021). https://doi.org/10.1002/admi.202002181.

[47] A. Ungureanu, B. Dragoi, V. Hulea, T. Cacciaguerra, D. Meloni, V. Solinas, E. Dumitriu, Effect of aluminium incorporation by the “pH-adjusting” method on the structural, acidic and catalytic properties of mesoporous SBA-15, Microporous and Mesoporous Materials. 163 (2012) 51–64. https://doi.org/10.1016/j.micromeso.2012.05.007.

[48] J. Socci, A. Osatiashtiani, G. Kyriakou, T. Bridgwater, The catalytic cracking of sterically challenging plastic feedstocks over high acid density Al-SBA-15 catalysts, Appl Catal A Gen. 570 (2019) 218–227. https://doi.org/10.1016/j.apcata.2018.11.020.

[49] B.A. Morrow, A.J. McFarlan, Surface vibrational modes of silanol groups on silica, J Phys Chem. 96 (1992) 1395–1400. https://doi.org/10.1021/j100182a068.

[50] V. Degirmenci, D. Uner, B. Cinlar, B.H. Shanks, A. Yilmaz, R.A. Van Santen, E.J.M. Hensen, Sulfated zirconia modified SBA-15 catalysts for cellobiose hydrolysis, Catal Letters. 141 (2011) 33–42. https://doi.org/10.1007/s10562-010-0466-1.

[51] J.M.R. Gallo, C. Bisio, G. Gatti, L. Marchese, H.O. Pastore, Physicochemical characterization and surface acid properties of mesoporous [Al]-SBA-15 obtained by direct synthesis, Langmuir. 26 (2010) 5791–5800. https://doi.org/10.1021/la903661q.

[52] C. Morterra, G. Magnacca, A case study: surface chemistry and surface structure of catalytic aluminas, as studied by vibrational spectroscopy of adsorbed species, 1996.

[53] M. Grahn, A. Faisal, O.G.W. Öhrman, M. Zhou, M. Signorile, V. Crocellà, M.S. Nabavi, J. Hedlund, Small ZSM-5 crystals with low defect density as an effective catalyst for conversion of methanol to hydrocarbons, Catal Today. 345 (2020) 136–146. https://doi.org/10.1016/j.cattod.2019.09.023.

[54] C.A. Emeis, Determination of Integrated Molar Extinction Coefficients for Infrared Absorption Bands of Pyridine Adsorbed on Solid Acid Catalysts, J Catal. 141 (1993) 347–354. https://doi.org/10.1006/jcat.1993.1145.

[55] J. Aguado, D.P. Serrano, G. San Miguel, Analysis of products generated from the thermal and catalytic degradation of pure and waste polyolefins using Py-GC/MS, J Polym Environ. 15 (2007) 107–118. https://doi.org/10.1007/s10924-007-0051-x.

[56] L.O. Mark, M.C. Cendejas, I. Hermans, The Use of Heterogeneous Catalysis in the Chemical Valorization of Plastic Waste, ChemSusChem. 13 (2020) 5808–5836. https://doi.org/10.1002/cssc.202001905.

[57] D.P. Serrano, J. Aguado, J.M. Escola, Developing advanced catalysts for the conversion of polyolefinic waste plastics into fuels and chemicals, ACS Catal. 2 (2012) 1924–1941. https://doi.org/10.1021/cs3003403.

CRediT authorship contribution statement

Valeria Finelli: Methodology, Validation, Investigation, Data Curation, Writing - Original Draft.

Valentina Gentilin: Methodology, Validation, Investigation.

Giulia Mossotti: Methodology, Validation, Investigation.

Gabriele Ricchiardi: Conceptualization, Methodology, Writing - Review & Editing

Alessandro Piovano: Conceptualization, Methodology, Validation, Investigation, Data Curation Writing - Review & Editing, Visualization, Supervision.

Valentina Crocellà: Conceptualization, Methodology, Validation, Investigation, Data Curation Writing - Review & Editing, Visualization, Supervision.

Elena Groppo: Conceptualization, Resources, Validation, Investigation, Data Curation Writing Review & Editing, Visualization, Supervision, Project administration, Founding acquisition.

Declaration of Competing Interest

The authors declare that they have no known competing financial interests or personal relationships that could have appeared to influence the work reported in this paper.

Graphical abstract

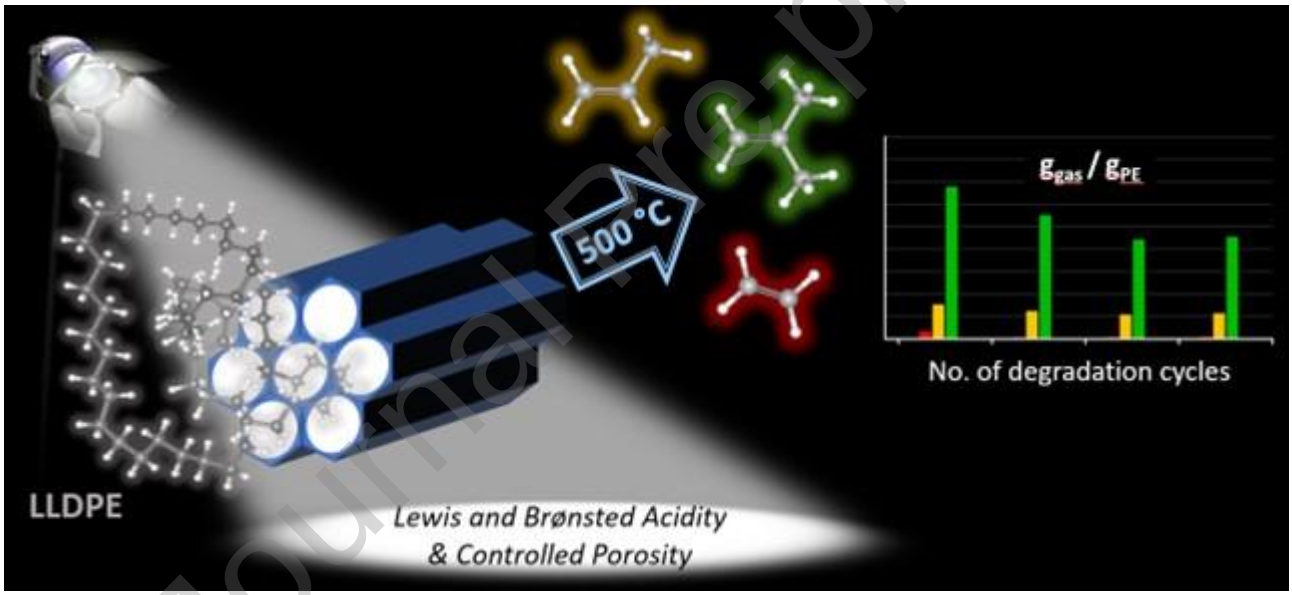

HIGHLIGHTS

- One-pot synthesis of ordered mesoporous silicas, pure or with heteroatoms (Zr or Al).
- LLDPE catalytic pyrolysis in batch reactor for volatile products.
- Good correlation between lowering of degradation temperature and products yield.
- Fundamental role of Brønsted acid sites in the catalytic process.
- Not only the amount of acid sites is important, but also the type and strength.